

Helical Twisting Number and Braiding Linkage Number of Solar Coronal Loops

Markus J. Aschwanden¹

¹) *Lockheed Martin, Solar and Astrophysics Laboratory, Org. A021S, Bldg. 252, 3251 Hanover St., Palo Alto, CA 94304, USA; e-mail: aschwanden@lmsal.com*

ABSTRACT

Coronal loops in active regions are often characterized by quasi-circular and helically twisted (sigmoidal) geometries, which are consistent with dipolar potential field models in the former case, and with nonlinear force-free field models with vertical currents in the latter case. Alternatively, Parker-type nanoflare models of the solar corona hypothesize that a braiding mechanism operates between unresolved loop strands, which is a more complex topological model. In this study we use the vertical-current approximation of a nonpotential magnetic field solution (that fulfills the divergence-free and force-free conditions) to characterize the number of helical turns N_{twist} in twisted coronal loops. We measure the helical twist in 15 active regions observed with AIA and HMI/SDO and find a mean nonpotentiality angle (between the potential and nonpotential field directions) of $\mu_{NP} = 15^\circ \pm 3^\circ$. The resulting mean rotational twist angle is $\varphi = 49^\circ \pm 11^\circ$, which corresponds to $N_{twist} = \varphi/360^\circ = 0.14 \pm 0.03$ turns with respect to the untwisted potential field, with an absolute upper limit of $N_{twist} \lesssim 0.5$, which is far below the kink instability limit of $|N_{twist}| \gtrsim 1$. The number of twist turns N_{twist} corresponds to the Gauss linkage number N_{link} in braiding topologies. We conclude that any braided topology (with $|N_{link}| \geq 1$) cannot explain the observed stability of loops in a force-free corona, nor the observed low twist number. Parker-type nanoflaring can thus occur in non-forcefree environments only, such as in the chromosphere and transition region.

Subject headings: Sun: corona — Sun: magnetic fields — magnetic reconnection

1. INTRODUCTION

In this study we are measuring physical parameters of coronal loops that are useful as observational constraints for testing of theoretical coronal heating models, such as the observed helical twist number of loops. These measurements should clarify whether the magnetic field in the solar corona exhibits sufficient helical twisting so that it can be described by a braiding topology, which plays a key role in Parker-type nanoflare-driven heating scenarios (Parker 1988).

Observations of the coronal magnetic field that have been interpreted in terms of helically twisted or braided topologies include flux ropes (Rust and Kumar 1996; Gary and Moore 2004; Raouafi 2009), coronal loops (Török and Kliem 2003; Török et al. 2010; Prior and Berger 2012), spiral structures in the transition region (Huang et al. 2018), chromospheric tornadoes (Wedemeyer-Böhm et al. 2012), emerging active regions (Liu and Schuck 2012), coronal mass ejections (Kumar et al. 2012), eruptive filaments/prominences (Kumar et al. 2010; Koleva et al. 2012), confined eruptions (Hassanin and Kliem 2016), and possibly braided finestructure in Hi-C observations (Winebarger et al. 2013, 2014; Cirtain et al. 2013; Tiwari et al. 2014; Pant et al. 2015).

First clear evidence for helically kinked magnetic flux ropes was found by Rust and Kumar (1996), based on the sigmoid (S-shaped or Z-shaped) geometry of 103 transient loop structures observed in soft X-rays by Yohkoh. Evidence for a multiple-turn helical magnetic flux tube that was erupting during a flare was suggested by Gary and Moore (2004), in a singular case. Also, a double-turn geometry in an erupting filament was suggested by Kumar et al. (2010) in another single case.

However, direct measurements of braiding parameters (such as the number of helical twisting turns or the Gauss linkage number) have only been attempted in very few single cases (Portier-Foazzani et al. 2001; Malanushenko et al. 2011, 2012; Thalmann et al. 2014). The measured helical twist is a very important quantity, because a magnetic topology can only be diagnosed as a braiding mechanism when it produces multiple helical turns, which dis-qualifies phenomena that exhibit a fraction of a single helical turn only. In this Paper we determine the helical twist number in active regions, using a newly developed nonlinear force-free field code that is parameterized in terms of the helical twist of unipolar magnetic charges, the so-called *vertical-current approximation nonlinear force-free field (VCA-NLFFF)* code. A similar concept was previously applied using a Grad-Rubin-type NLFFF code (Malanushenko et al. 2011, 2012), and the Wiegmann-NLFFF code (Thalmann et al. 2014).

The content of this Paper contains a brief theoretical description of the VCA-NLFFF code (Section 2.1), the braiding topology and linkage number (Section 2.2), and the kink and torus instability (Section 2.3). Then we carry out data analysis of AIA and HMI observations that is specifically designed to measure the helical twist and the Gauss linkage number (Section 3), followed by a discussion (Section 4) and conclusions (Section 5).

2. THEORY

2.1. Nonlinear Force-Free Magnetic Field

A physically valid coronal magnetic field solution has to satisfy Maxwell’s equations, which includes the divergence-freeness condition,

$$\nabla \cdot \mathbf{B} = 0 , \quad (1)$$

and the force-freeness condition,

$$\nabla \times \mathbf{B} = \alpha(\mathbf{r})\mathbf{B} , \quad (2)$$

where $\alpha(\mathbf{r})$ represents a scalar function that depends on the position \mathbf{r} , but is constant along a magnetic field line. Three different types of magnetic fields are generally considered for applications to the solar corona: (i) a *potential field (PF)* where the α -parameter vanishes ($\alpha = 0$), (ii) a *linear force-free field (LFFF)* ($\alpha = \text{const}$), and (iii) a *nonlinear force-free field (NLFFF)* with a spatially varying $\alpha(\mathbf{r}) \neq 0$.

Due to the axi-symmetry of a divergence-free flux tube, it is useful to write the divergence-free condition (Eq. 1) and the force-free condition (Eq. 2) in spherical coordinates (r, θ, φ) , expressed with the magnetic field components $(B_r, B_\theta, B_\varphi)$, where r is the radial direction, θ the inclination angle, and φ the azimuth angle (Fig. 1a,b),

$$(\nabla \cdot \mathbf{B}) = \frac{1}{r^2} \frac{\partial}{\partial r}(r^2 B_r) + \frac{1}{r \sin \theta} \frac{\partial}{\partial \theta}(B_\theta \sin \theta) + \frac{1}{r \sin \theta} \frac{\partial B_\varphi}{\partial \varphi} = 0 , \quad (3)$$

$$[\nabla \times \mathbf{B}]_r = \frac{1}{r \sin \theta} \left[\frac{\partial}{\partial \theta}(B_\varphi \sin \theta) - \frac{\partial B_\varphi}{\partial \varphi} \right] = \alpha B_r , \quad (4)$$

$$[\nabla \times \mathbf{B}]_\theta = \frac{1}{r} \left[\frac{1}{\sin \theta} \frac{\partial B_r}{\partial \varphi} - \frac{\partial}{\partial r}(r B_\varphi) \right] = \alpha B_\theta , \quad (5)$$

$$[\nabla \times \mathbf{B}]_\varphi = \frac{1}{r} \left[\frac{\partial}{\partial r}(r B_\theta) - \frac{\partial B_r}{\partial \theta} \right] = \alpha B_\varphi . \quad (6)$$

Due to the nonlinearity of the equation system, no general analytical solution of the magnetic field $\mathbf{B}(\mathbf{r})$ has been obtained for the coupled equation system of Eqs.(1-2) or Eqs.(3-6). However, an analytical approximation of a divergence-free and force-free magnetic field solution has been derived for a vertical current at the lower photospheric boundary, which twists a field line into a helical shape (Aschwanden 2013a),

$$B_r(r, \theta) = B_0 \left(\frac{d^2}{r^2} \right) \frac{1}{(1 + b^2 r^2 \sin^2 \theta)} , \quad (7)$$

$$B_\varphi(r, \theta) = B_0 \left(\frac{d^2}{r^2} \right) \frac{br \sin \theta}{(1 + b^2 r^2 \sin^2 \theta)} , \quad (8)$$

$$B_\theta(r, \theta) \approx 0 , \quad (9)$$

$$\alpha(r, \theta) = \frac{2b \cos \theta}{(1 + b^2 r^2 \sin^2 \theta)} \approx 2b , \quad (10)$$

$$b = \frac{2\pi N_{twist}}{L} = \frac{\varphi}{L} , \quad (11)$$

where B_0 is the magnetic field strength vertically above a buried magnetic charge at photospheric height, d is the depth of the buried magnetic charge, L is the length of a magnetic field line, and $b = \varphi/L$ is related to the azimuthal rotation angle φ , from which the number N_{twist} of helical turns can be calculated. The accuracy of the analytical approximation can be verified by inserting the solution of Eqs. (7-10) into the equation system of Eqs. (3-6), which shows that all linear terms $\propto br \sin \theta$ cancel out exactly, so that only second-order terms $\propto b^2 r^2 \sin^2 \theta$ remain. Thus the approximation is most accurate for a near-potential field solution with $|br \sin \theta| \ll 1$. Note that the analytical solution of Eq. (7-8) represents a generalization of the solution for a straight (not divergence-free) flux tube with uniform twist (e.g., see textbooks by Priest 1982, 2014; Sturrock 1994; Boyd and Sanderson 2003; Aschwanden 2004).

We see that the nonpotential solution ($b \neq 0$) degenerates to the potential field solution in the case of ($b = 0$),

$$B_r(r) = B_0 \left(\frac{d_j}{r_j} \right)^2 . \quad (12)$$

The 3-D vector field of the magnetic field is then,

$$\mathbf{B}_j(\mathbf{x}) = B_j \left(\frac{d_j}{r_j} \right)^2 \frac{\mathbf{r}_j}{r_j} , \quad (13)$$

Such a magnetic field model with a single buried magnetic (unipolar) charge can be adequate for a sunspot. For a bipolar active region, at least two magnetic charges with opposite magnetic polarities are necessary.

A general magnetic field can be constructed by superposing the n_{mag} fields of $j = 1, \dots, n_{mag}$ magnetic charges, defined as,

$$\mathbf{B}(\mathbf{x}) = \sum_{j=1}^{n_{mag}} \mathbf{B}_j(\mathbf{x}) = \sum_{j=1}^{n_{mag}} B_j \left(\frac{d_j}{r_j} \right)^2 \frac{\mathbf{r}_j}{r_j} . \quad (14)$$

where the depth d_j of a magnetic charge j is,

$$d_j = 1 - \sqrt{x_j^2 + y_j^2 + z_j^2} , \quad (15)$$

and the distance r_j between the magnetic charge position (x_j, y_j, z_j) and an arbitrary location (x, y, z) where the calculation of a magnetic field vector is desired, is defined by,

$$r_j = \sqrt{(x - x_j)^2 + (y - y_j)^2 + (z - z_j)^2} . \quad (16)$$

The origin at the spherical coordinate system is chosen at the center of the Sun, while the sub-photospheric location of a buried magnetic charge is defined at the position (x_j, y_j, z_j) , the vertical direction ($\theta = 0$) is perpendicular to the solar surface, and the physical unit of length scales (such as d_j in Eq. 15 and r_j in Eq. 16) is in solar radii.

The multi-pole magnetic field is divergence-free, since

$$\nabla \cdot \mathbf{B} = \nabla \cdot \left(\sum_j \mathbf{B}_j \right) = \sum_j (\nabla \cdot \mathbf{B}_j) = 0 , \quad (17)$$

while the force-freeness is fulfilled with second-order accuracy in ($\propto b^2 r^2 \sin^2 \theta$) for the solution of the vertical-current approximation of Eqs. (3)-(6) (Aschwanden 2013a),

$$\nabla \times \mathbf{B} = \nabla \times \sum_{j=1}^{N_m} \mathbf{B}_j \approx \sum_{j=1}^{N_m} (\nabla_j \times \mathbf{B}_j) = \sum_{j=1}^{N_m} \alpha_j(\mathbf{r}) \mathbf{B}_j = \alpha(\mathbf{r}) \mathbf{B} . \quad (18)$$

Numerical tests of comparing the analytical approximation solution with other nonlinear force-free field codes have been conducted for a large number of simulated and observed magnetograms, and satisfactory agreement with other NLFFF codes has been established (e.g., Aschwanden 2013a, 2013b, 2016; Aschwanden and Malanushenko 2013; Warren et al. 2018).

Note that 4 free parameters are required for a potential field solution (x_j, y_j, z_j, B_j) , and 5 free parameters for a nonpotential solution, i.e., $(x_j, y_j, z_j, B_j, b_j)$, for every magnetic unipolar charge j . A key parameter for the investigation of field twisting and braiding studied here, is the number N_{twist} of helical turns of a loop, which can be calculated from the length L_j of a magnetic field line (that represents the axis of a loop), and the associated nonlinear parameter b_j (Eq. 11),

$$N_{twist} = \frac{b_j L_j}{2\pi} = \frac{\varphi_j}{2\pi} , \quad (19)$$

where φ_j is the rotation angle of a twisted loop. The relationship between the potential field component B_P , the nonpotential field component B_{NP} , and the azimuthal magnetic field component B_φ is depicted in Fig. (1c), which defines the so-called *nonpotentiality angle* μ_{NP} between the potential and nonpotential field direction. The Pythagorean theorem of a rectangular triangle yields then,

$$B_{NP}^2 = B_P^2 + B_\varphi^2 , \quad (20)$$

which together with the magnetic energy definition $E = B^2/8\pi$ is consistent with the definition of the free energy $E_{free} = E_\varphi$ (Aschwanden 2013b),

$$E_{NP} = E_P + E_\varphi = E_P + E_{free} . \quad (21)$$

We can now calculate the nonpotentiality angle μ_{NP} from the energy ratio (E_P/E_{NP}), or from the mean magnetic field ratio (B_P/B_{NP}) (see geometrical relationship in Fig. 1c),

$$\mu_{NP} = \arccos \left(\sqrt{\frac{E_P}{E_{NP}}} \right) = \arccos \left(\frac{B_P}{B_{NP}} \right). \quad (22)$$

While the rotation angle $\varphi = 2\pi N_{twist}$ (Eq. 19) produces the helical twist of loops, the resulting nonpotentiality angle μ_{NP} between potential and nonpotential field lines can be expressed as (see geometrical relationship in Fig. 1c),

$$\mu_{NP} = \arctan \left(\frac{\varphi r}{L} \right) = \arctan \left(2\pi N_{twist} \frac{r}{L} \right), \quad (23)$$

where r is the radius of the azimuthal field strength $B_\varphi(r)$ dependence dropping to about half of its peak value. Theoretical calculations yield $r/L \approx 0.1 - 0.4$ (Fig. 4 in Aschwanden 2013a), which yields an estimated ratio of $\mu_{NP}/\varphi \approx (0.1 - 0.4)$ and can be tested with the alternative definition of Eq. (22). Equating Eqs. (22) and (23) yields the relationship between magnetic field ratio (B_P/B_{NP}) and the twist angle $\varphi r/L$, according to the geometrical relationship shown in Fig. 1c.

The main caveat of the VCA-NLFFF code is the limited accuracy of magnetic field modeling for large helical twist numbers (say for $N_{twist} \gtrsim 2$). A pathological case is the Gold-Hoyle flux rope (Gold and Hoyle 1960), which has been modeled for twist numbers $N_{twist} = 0, 1, 2, 3, 4, 5$ (Aschwanden 2013a, Appendix A). It reveals unrealistic distortions for large twist numbers $N_{twist} \gtrsim 2$, and thus indicates a breakdown of the approximation made in the VCA-NLFFF code, for such extreme cases. This limitation, however, does not affect the relatively high accuracy of the active regions analyzed here, which all consistently yield a low value of $N_{twist} \approx 0.1 - 0.2$. Moreover, the Gold-Hoyle flux rope exceeds the kink instability criterion, and thus may be not relevant for stable loops.

2.2. Braiding Topology and Linkage Number

While the previous section quantifies helically twisted structures, we turn now to braided (coronal) structures. The topology of braiding can be characterized by the so-called *Gauss linkage (or linking) number* N_{link} , which is defined as follows: *The linkage number is a topological parameter describing two curves that does not change as the curves are distorted without crossing through each other* (e.g., Priest 2014). Each curve is given a direction, and reversing one of the directions changes the linkage number N_{link} by (-1) . Each crossing has a sign $(+1)$ or (-1) , depending on whether the first curve is in front or behind the other, and the linkage number is half the sum of the signed crossings. Related to the linkage number is the magnetic helicity (for definitions see, e.g., Priest 2014). We will just use the linkage number here, which represents the number of times that each curve winds around the other (Fig. 2). If the two linked curves are closed, the linkage number is an integer number, while it can be generalized to a non-integer number for open curves (e.g., Démoulin et al. 2006 and references therein).

A braiding process is clearly recognizable when two curvi-linear structures exhibit at least 1-3 turns around each other (Fig. 2), so we will require a minimum linkage number of $|N_{link}| \geq 1$ for the identification of a braiding process, which is a strict lower limit for closed curves (since a non-zero integer number is required). Magnetic field lines in the solar corona are generally open curves, whose braiding can be characterized by non-integer numbers. If this linkage number in closed curves is less than unity, we will call it *helically twisted loops*, rather than *braided loops*. Fortunately, our parameterization of a nonlinear force-free magnetic field solution provides the number of helical twists, N_{twist} (Eq. 19), which we can directly compare with the

linkage number N_{link} of braiding. Four examples are visualized in Fig. (2), showing two parallel loop strands with no braiding (which has a Gauss linkage number of $L = 0$), a helically twisted loop with $L = 1$, and braided loop strands with linkage numbers of $L = 2$ and $L = 3$. Each loop can be distorted (e.g. by fitting a loop geometry to an observed magnetic field model), but does not change its linkage number L as long the number of mutual crossing points is not changed. In the four examples shown in Fig. (2) we have chosen integers for the linkage numbers, but it is trivial to adjust for non-integer numbers in loop pairs with open curves.

2.3. Kink and Torus Instability

Testing the (circular and helical) loop structures observed in the solar corona, we have to address their stability. Circular loops generally indicate a near-potential magnetic field, which tends to be stable, while sigmoid structures indicate a nonpotential magnetic field, possibly being unstable. Since the potential field solution represents the (magnetic) energy minimum configuration, we would expect that potential fields are perfectly stable, while non-potential fields have free energy that can be dissipated and thus the loops are not necessarily stable. On the other side, the magnetic field solution that we derived with the vertical-current approximation method (Eqs. 7-11) is divergence-free and force-free (to second-order accuracy), and thus the force-freeness indicates a stable or a marginally stable condition.

However, it was recognized early on that force-free flux tubes can be prone to the helical kink instability (e.g., see textbook by Priest 2014, p.266), or to the torus instability (e.g., Kliem and Török 2006; Isenberg and Forbes 2007), if the helical twist exceeds about one turn. The detailed instability criterion depends on additional conditions, such as the axial magnetic field, the plasma pressure gradient, magnetic field line curvature, and line-tying. Hood and Priest (1979) calculated the kink instability criterion for a force-free field and uniform twist to be 3.3π , which corresponds to $N_{twist} = 3.3\pi/2\pi = 1.65$ turns, while this value was found to vary in a typical range of $N_{twist} \approx 1 - 3$ for other magnetic field configurations. Further calculations including the line-tying effect of the dense photosphere yielded a threshold of 2.5π or $N_{twist} = 2.5\pi/2\pi = 1.25$ turns (Hood and Priest 1981).

The evolution of twisting coronal magnetic flux tubes with a compressible zero-beta, ideal MHD code has been simulated, which showed the formation of a helically twisted flux tube that evolved along a sequence of force-free equilibria with progressively stronger helical twist. The system becomes unstable for a critical twist of $2.5\pi \leq \Phi_c \leq 2.75\pi$, which corresponds to $N_{twist} = 1.25 - 1.38$ turns (Török and Kliem 2003).

A similar process observed in laboratory plasmas (in tokamaks and spheromacs) is the torus instability, an expansion instability of a toroidal current ring, for which an equilibrium was established by Shafranov, (called the Kruskal-Shafranov limit $k \geq -\Phi/L$). Qualitative agreement between spheromak experiments and solar coronal mass ejections was pointed out by Kliem and Török (2006). Further MHD simulations of an embedded flux rope showed the formation of an aneurism-like structure when it erupts, which was identified as torus instability (Isenberg and Forbes 2007). MHD simulations of magnetic reconnection in a kinking flux rope were also performed with high initial twist ($\Phi \gtrsim 6\pi$), which corresponds to $N_{twist} = 6\pi/2\pi = 3$ helical turns (Kliem et al. 2010), but such a configuration with multiple helical turns has never been reported from solar observations in non-flaring conditions. There was one single observation reported of a multiple-turn spiral flux tube with about 4 turns (Gary and Moore 2004), which occurred during an eruption from an active region, but its morphology could equally well be interpreted as a (quasi-periodic) chain of multiple vortices of the Kelvin-Helmholtz instability (Aschwanden 2019, Section 11.8).

In summary, there is strong evidence that loop structures in the force-free corona do not exhibit helical twisting with more than one turn, while multiple helical turns, which would be required for a coronal braiding process, are inherently unstable to the kink or torus instability, as demonstrated by analytical calculations and numerical MHD simulations.

3. DATA ANALYSIS

3.1. Active Regions Observed with SDO

We analyze a data set of 15 active regions observed with AIA/SDO and HMI/SDO, which is identical to the selection made in recent studies by Warren et al. (2012, 2018). The first study (Warren et al. 2012) contains a *differential emission measure (DEM)* analysis of EIS/Hinode data in the temperature range of $T_e \approx 1 - 10$ MK. The second study (Warren et al. 2018) compares three different magnetic field extrapolation codes. The times and heliographic positions of the analyzed 15 active regions are given in Table 1.

3.2. Data Analysis Method

The basic feature that is unique to our magnetic field modeling method is the inclusion of the observed geometry of coronal loop structures from EUV images, besides the photospheric magnetograms $B_z(x, y)$, while the transverse components $B_x(x, y)$ and $B_y(x, y)$ are ignored due to their larger uncertainties than the line-of-sight component $B_z(x, y)$, partially caused by the non-forcefreeness of the magnetic field in the photosphere and lower chromosphere. This magnetic field extrapolation code makes use of the vertical-current approximation of the nonpotential field, called the VCA-NLFFF code. A description, performance tests, and measurements of magnetic free energies is given in Aschwanden (2016), the theory in Aschwanden (2013a), numerical simulations and tests in Aschwanden and Malanushenko (2013), the free energy concept in Aschwanden (2013b), additional applications to STEREO data in Sandman et al. (2009), Aschwanden and Sandman (2010), Sandman and Aschwanden (2011), Aschwanden et al. (2012, 2015), Aschwanden (2013c), comparisons with other NLFFF codes in Aschwanden et al. (2014a), Warren et al. (2018), and applications to IRIS, IBIS, and ROSA data in Aschwanden (2015) and Aschwanden et al. (2016). The VCA-NLFFF code is also publicly available in the SSW library encoded in the *Interactive Data Language (IDL)*, see website <http://www.lmsal.com/~aschwand/software/>.

3.3. Input Parameters

We show an example of a VCA-NLFFF run in Fig. 3, which refers to event #14 (listed in Table 1). Each of the 15 analyzed images encompasses an active region, within a field-of-view of $FOV = 0.47 \pm 0.08 R_\odot$. The input parameters of event #14 (listed on the right side of Fig. 3) includes the instrument (AIA, with the wavelengths 94, 131, 171, 193, 211, 335 Å), the NOAA active region number 11339, and the heliographic position at the center of the image, N20W03. The automated loop detection with the OCCULT-2 code (Aschwanden, De Pontieu and Katrukha 2013) is controlled by a few tuning parameters, such as the maximum acceptable misalignment angle ($a_{mis} = 20^\circ$), the lowpass filter ($n_{sm1}=1$ pixel), the highpass filter ($n_{sm2}=n_{sm1}+2=3$ pixels), the maximum number of magnetic source components ($n_{mag} = 30$), the maximum number of detected structures ($N_{struc} = 1000$), the minimum and maximum number of iterations

($n_{itmin} = 10$, $n_{itmax} = 50$), the proximity limit between a detected loop position and a magnetic charge ($prox_{min} < 10$ magnetic source depths), the minimum loop length ($l_{min} = 5$ pixels), the minimum curvature radius ($r_{min} = 8$ pixels), the flux threshold ($q_{thresh1} = 0$), and the bipass-filtered flux threshold ($q_{thresh2} = 0$).

The VCA-NLFFF code executes 3 major tasks: (i) the decomposition of a magnetogram $B_z(x, y)$ into a finite number of magnetic sources, characterized by their sub-photospheric positions (x_j, y_j, z_j) , $j = 1, \dots, n_{mag}$, and the surface magnetic field strength vertically above the buried unipolar magnetic charge (B_j); (ii) the automated tracing of curvi-linear structures in multiple wavelength bands (here from 6 AIA images in coronal wavebands); and (iii) forward-fitting of the nonlinear force-free α -parameters $a_j \approx 2b_j$, which is an optimization algorithm that minimizes the misalignment angles μ between the observed loop directions and the theoretically calculated magnetic field lines.

3.4. Output Parameters

For event #14 (Fig. 3) we find a number of $n_{det} = 483$ automatically detected loop structures, of which $n_{loop} = 280$ loops have a misalignment angle below the limit of $a_{mis} = 20^\circ$. Larger misangle limits have also been tested, but yielded similar results, except for an increase of mis-identifications of curvi-linear features such as moss. The total magnetic potential field energy of the entire active region amounts to $E_P = 2.5 \times 10^{33}$ erg, and the ratio of the nonpotential to the potential energy is a factor of $E_{NP}/E_P = 1.145$, which implies a free energy of $\approx 15\%$. Comparing among the 15 active regions listed in Table 1, we see that event #14 has the largest nonpotential energy ratio. From the histogram of misalignment angles (Fig. 3 top right) we see that the 2-D misalignment angle has a median of $\mu_2 = 6.8^\circ$, which is measured from the line-of-sight projected loop coordinates. However, from our 3-D best-fit model we can derive also a 3-D misalignment angle, which has a value of $\mu_3 = 12.4^\circ$. These misalignment angles tell us how well the theoretical magnetic field model converges to the observed loop geometries.

3.5. Helical Twist Analysis

Since the vertical-current approximation concept produces helically twisted field lines by definition, we can now determine various parameters of the helical twist. From the energy ratio E_P/E_{NP} we can directly measure the nonpotentiality angle between the potential and nonpotential field by using Eq. (22), for which we find a value of $\mu_{NP} = 20.8^\circ$ (for event #14), or $\mu_{NP} = 14.7^\circ \pm 2.8^\circ$ in the statistical average of all 15 analyzed active regions. These values are based on the energy ratios that have a statistical average of $E_{NP}/E_P = 1.07 \pm 0.03$ (Table 1).

The helical twist can be expressed by the average rotation angle $\varphi_j = b_j L_j$, $j = 1, \dots, n_{loop}$ (Eq. 19), which depends on the measurement of the nonlinear α -parameters $a_i \approx 2b_i$, $i = 1, \dots, n_{mag}$ (Eq. 10). However, since the location of a detected loop is independent of the location of magnetic sources, we have to calculate the α -parameter a_j , $j = 1, \dots, n_{loop}$ from the nearest magnetic charge a_i , $i = 1, \dots, n_{mag}$. Averaging then all rotation angles $\varphi_j = b_j L_j$, $j = 1, \dots, n_{loop}$ we find for event #14 a mean rotation angle of $\varphi = 69^\circ \pm 47^\circ$, which corresponds to a number of twists, $N_{twist} = \varphi/360^\circ = 0.19 \pm 0.13$, which is a fifth of a full turn only, although this active region has the largest helical twist. The average of all 15 active regions exhibit a mean rotation twist angle of $\varphi = 49^\circ \pm 11^\circ$, or number of twist $N_{twist} = 0.14 \pm 0.03$ (Table 1). The length L_j has been measured along a field line from the first to the second footpoint for closed loops, while L_j was limited by the height range ($L_j \leq h_{max} = 0.2R_\odot$) of the computation box for open field lines.

The distributions of the helical twist numbers N_{twist} are shown separately for each of the 15 analyzed active regions (listed in Table 1), which exhibit that their values are always much smaller than a half turn, i.e., $N_{twist} \lesssim 0.5$ (Fig. 4), and have a mean of $N_{twist} \approx 0.14 \pm 0.03$, which is much less than the kink or torus instability criterion ($|N_{kink}| \gtrsim 1$), as well as far below any loop braiding scenario ($|N_{link}| \geq 1$).

4. DISCUSSION

4.1. Helical Twist Measurements

It was noticed that the projected geometry of a helically twisted flux tube is a sigmoid (or S-shape), most prominently displayed in SXT/Yohkoh images (Rust and Kumar 1996) and in EIT/SOHO images (Portier-Fozzani et al. 2001). Also it was known since early on that a flux tube is prone to the kink instability if the twisting exceeds about a full turn, $N_{twist} \gtrsim 1$. Based on this criterion one expects stability below this value, and an eruptive behavior above this value, and thus eruptions can be predicted from the value of the twisting number during any time evolution. Although such a critical parameter is very useful, no method has been developed until recently that would facilitate quantitative measurements of the helical twist.

Portier-Fozzani et al. (2001) developed a forward-fitting method that fitted a parameterized helical field line that is wound around a circular torus, to loop shapes observed with EIT, using the solar rotation stereoscopy method (for a review see Aschwanden 2011), and tracked the evolution of the twist angle as a function of time. The twist evolved from $N_{twist} = 210^\circ/360^\circ = 0.58$ to $N_{twist} = 10^\circ/360^\circ = 0.03$ over the period of one day, which indicates a relaxation of the nonpotential magnetic field.

Malanushenko et al. (2011, 2012) carries out forward-fitting of a linear force-free field to individual loops detected in EUV images, in order to obtain the nonlinear α -parameter that determines the helical twist number. The time evolution of the so-determined magnetic helicity in the corona can then be compared to that of the magnetic flux helicity across the photosphere, which were found to be similar.

Thalmann et al. (2014) measure the evolution of the free (magnetic) energy in an active region observed with Hi-C, using the Wiegmann-NLFFF code (Wiegmann et al. 2006). The free energy is calculated from the azimuthal magnetic field component $B_\varphi(t)$, i.e., $E_\varphi(t) = B_\varphi^2(t)V/8\pi$. They find that the overall twist of the flux rope increased by about half a turn within 12 minutes, from $N_{twist} \approx 1.0$ to $N_{twist} \approx 1.5$. These latter values appear to be close to the kink instability criterion.

The first method (Portier-Fozzani et al. 2001) represents a geometrical fit without magnetic field constraints, while the second (Malanushenko et al. 2011, 2012) and third method (Thalmann et al. 2014) are based on forward-fitting of a *linear force-free field (LFFF)* magnetic field model, which constrains the helical twist of a single loop or loop bundle. In comparison, our VCA-NLFFF method fits the nonlinear α -parameter for every loop bundle that is associated with a unipolar magnetic charge. @ In future work, it will be @ straightforward to study the evolution of each unipolar @ magnetic charge in an active region separately, and @ to predict eruptions in individual unstable zones of an @ active region. A similar partitioning of unipolar magnetic regions, along with a decomposition into “spin helicity” and “braiding helicity”, has been modeled in Longcope et al. (2007).

4.2. Coronal Braiding

Hi-C observations have been claimed to be the first direct evidence of braided magnetic fields in the solar corona (Winebarger et al. 2013, 2014; Cirtain et al. 2013; Tiwari et al. 2014; Pant et al. 2015). These observations show nanoflare-like time evolutions in inter-moss loops (Winebarger et al. 2013, 2014), finestructures down to $0.2''$ scales (Cirtain et al. 2013), external triggering of coronal subflares in active regions (Tiwari et al. 2014), and quasi-periodic flows with velocities of $13\text{--}185\text{ km s}^{-1}$ (Pant et al. 2015), apparently occurring in braided finestructure. However, no helical twist number or Gauss linkage number has been measured in these high(est)-resolution Hi-C observations that could provide a quantitative proof of the hypothesized braiding topology and geometry. Although it has been argued that braided finestructure are unresolved by current instruments, the recent observations with Hi-C (with a pixel size of $\approx 0.1''$) have convincingly demonstrated that AIA resolves many of the loops (Peter et al. 2013; Brooks et al. 2013, 2016; Morton and McLaughlin 2013; Aschwanden and Peter 2017).

Although a few apparently braided structures have been detected in highpass-filtered 193 \AA images, numerical simulations of braided multi-thread bundles of coronal loops produce braiding at a range of scales, but the observed EUV intensities may not necessarily reveal the underlying braided topology (Wilmot-Smith et al. 2009; Pontin et al. 2017), especially once magnetic reconnection started (Wilmot-Smith et al. 2010, 2011; Yeates et al. 2010; Pontin et al. 2011).

A model with magnetic helicity condensation, based on the inverse cascade from small scales to large scales that is known from turbulent MHD systems, provides a mechanism that removes most complex fine structure from the rest of the corona, resulting in smooth and laminar loops (Antiochos 2013), which could be the reason that we do not see braided field lines in the Quiet Sun (Antiochos 2013; Kniznik et al. 2017).

Most of the 3-D MHD simulations of twisted coronal loops with random footpoint motion focus on the coronal heating rate (e.g., Wilmot-Smith et al. 2011; Yeates et al. 2014; Pontin and Hornig 2015; Bourdin et al. 2013, 2015; Hansteen et al. 2015; Peter 2015; Dahlburg et al. 2016; Reale et al. 2016), but the degree of twisting and/or braiding (topology), which is our main focus here, is largely unconstrained by observations in these MHD simulations.

The braiding topology has also been mimicked with a self-organized criticality model, which yields the result that the power law distributions of (avalanche) energies are altered by the presence of net helicity (Berger et al. 2009, 2015). This is consistent with the fact that free (magnetic) energy depends on the degree of helical twisting (Eqs. 20–21).

4.3. Photospheric/Chromospheric Braiding

The viability of a braiding mechanism has been simulated with magneto-convection simulations, where the topological complexity is quantified in terms of the field line winding, the finite time topological entropy, or passive scalar mixing. A benchmark test that infers photospheric flows from sequences of magnetograms with local correlation tracking shows that complex tangling of photospheric motions occurs on a time scale of hours, but no global net winding is induced (Ritchie et al. 2016; Candelaresi et al. 2018).

Numerical (resistive) MHD simulations of twisted and (more complex) braided magnetic fields show that both fields can relax to stable force-free equilibria, reaching force-free end states, but the electric current structures in these final states differ significantly between the (diffuse) braided field and the (sigmoidal) twisted field (Prior and Yeates 2016a, 2016b).

Photospheric magnetic braiding models with Alfvénic wave turbulence, in which the coronal field lines are subject to slow random footpoint motion, have been developed by van Ballegooijen et al. (2014, 2017), but the resulting coronal heating rate was found to be insufficient to balance the conductive and radiative losses, given the observed velocities ($v \approx 1 \text{ km s}^{-1}$) of the footpoint motions.

Magnetic field line braiding in the photosphere, chromosphere, and transition region is fundamentally different from the corona, because the latter is largely in a stable force-free state (except during flares or eruptive processes), while the former domains are located in non-forcefree zones, where turbulent MHD models are more appropriate than in the force-free corona.

5. CONCLUSIONS

In this study we measure the helical twist number of coronal field lines, which is identical to the Gauss linkage number in braiding topologies. Our conclusions are the following:

1. The vertical-current approximation nonlinear force-free field (VCA-NLFFF) code yields a mean non-potentiality angle of $\mu_{NP} = 15^\circ \pm 3^\circ$ for a set of 15 active regions, which is a quantitative measure how much nonpotential the average magnetic field is compared with a potential field. The related free energy ratio averages to a value of $E_{NP}/E_P = 1.07 \pm 0.03$, so the analyzed active regions have a free energy of $E_{free}/E_P \approx 4\% - 10\%$, which is consistent with a larger study of 173 events, where $E_{free}/E_P \approx 1\% - 25\%$ was found (Aschwanden, Xu, and Jing 2014b).
2. The mean nonpotentiality angle μ_{NP} corresponds of a mean rotational twist angle of $\varphi = 49^\circ \pm 11^\circ$, measured over the length of a field line, which corresponds to a relatively low twist number of $N_{twist} = 0.14 \pm 0.03$ turns. This is the first quantitative result of the helical twist number in the solar corona, based on nonlinear force-free magnetic modeling. A few linear force-free fits have been previously pioneered by Malanushenko et al. (2011, 2012) and Thalmann et al. (2014).
3. The helical twist number N_{twist} of a magnetic field line is equivalent to the Gauss linkage number N_{link} . Our result of a relatively small value of the helical twist number, i.e., $N_{twist} \approx 0.15$, is far below the kink instability or torus instability value $|N_{twist}| \approx 1.0$, and thus is consistent with the observed stability of coronal loops. An absolute upper limit of our measurements in (non-flaring) active regions is found to be a half turn ($N_{twist} \lesssim 0.5$).
4. Numerical 3-D MHD simulations with high linkage numbers $|N_{link}| \gtrsim 1$ are neither consistent with the observed low twist numbers, nor are they consistent with the observed stability of coronal loops.
5. Parker-type nanoflaring scenarios assume braiding of magnetic field lines, which then trigger magnetic reconnection above some threshold value of field line misalignment between adjacent field lines. However, no significant braiding ($N_{link} = 1, 2, \dots$) can build up in the force-free solar corona according to our observed helical twist numbers, and thus Parker-type nanoflaring is more likely to occur in non-forcefree environments, such as in the chromosphere and transition region, rather than in the force-free corona. Magneto-convection below and above the photosphere and the associated MHD turbulence is a viable driver for chromospheric nanoflaring.

Future progress in our understanding of coronal heating mechanisms strongly depends on accurate magnetic field models. Nonlinear force-free field models (NLFFF) have been criticized because of the non-forcefreeness of the lower boundary in the photosphere (DeRosa et al. 2009), but improvements have been

implemented by preprocessing of photospheric fields (Wiegelmann et al. 2006), forward-fitting to automatically traced coronal loops (Aschwanden 2013a), and magneto-static modeling (Wiegelmann et al. 2017). Nevertheless, the existing NLFFF codes are still not able to model satisfactorily the high-resolution data of Hi-C, although a faithful attempt has been made (Thalmann et al. 2014). It appears that many loop structures are resolved in Hi-C images (Peter et al. 2013; Brooks et al. 2013; Winebarger et al. 2013, 2014; Morton and McLaughlin 2013; Alexander et al. 2013; Tiwari et al. 2016; Aschwanden and Peter 2017). On the other side, high-resolution magnetic field measurements with HMI/SDO do not match up the resolution of Hi-C, but may be available with DKIST in near future (Tritschler et al. 2016).

We acknowledge useful discussions with Aad van Ballegooijen and attendees of a DKIST science planning meeting, held at Newcastle upon Tyne (UK). This work was partially supported by NASA contracts NNX11A099G, NNG04EA00C (SDO/AIA), and NNG09FA40C (IRIS).

References

- Alexander, C.E., Walsh, R.W., Regnier, S., Cirtain, J., Winebarger, A.R., et al. 2013, ApJ 775, L32. *Anti-parallel EUV Flows Observed along Active Region Filament Threads with Hi-C*
- Antiochos, S.K. 2013, ApJ 590, 547. *Helicity condensation as the origin of coronal and solar wind structure*
- Aschwanden, M.J.: 2004, *Physics of the Solar Corona. An Introduction*, Berlin: Springer and Praxis, p.216.
- Aschwanden, M.J. and Sandman, A.W. 2010, *Bootstrapping the coronal magnetic field with STEREO: Unipolar potential field modeling*, ApJ 140, 723.
- Aschwanden, M.J. 2011, Living Reviews in Solar Physics 8, 5. *Solar stereoscopy and tomography*
- Aschwanden, M.J., Wuelser, J.-P., Nitta, N.V., et al. 2012, *First 3D Reconstructions of Coronal Loops with the STEREO A and B Spacecraft: IV. Magnetic Field Modeling with Twisted Force-Free Fields*, ApJ 756, 124.
- Aschwanden, M.J. 2013a, SoPh 287, 323, *A nonlinear force-free magnetic field approximation suitable for fast forward-fitting to coronal loops. I. Theory*
- Aschwanden, M.J. 2013b, SoPh 287, 369. *A nonlinear force-free magnetic field approximation suitable for fast forward-fitting to coronal loops. III. The free energy*
- Aschwanden, M.J. 2013c, *Nonlinear force-free magnetic field fitting to coronal loops with and without stereoscopy*, ApJ 763, 115.
- Aschwanden, M.J. and Malanushenko, A. 2013, SoPh 287, 345. *A nonlinear force-free magnetic field approximation suitable for fast forward-fitting to coronal loops. II. Numerical Code and Tests*
- Aschwanden, M.J., DePontieu, B., and Katrukha, E. 2013, *Optimization of Curvi-Linear Tracing Applied to Solar Physics and Biophysics*, Entropy, 15(8), 3007.
- Aschwanden, M.J., Sun, X.D., and Liu, Y. 2014a, *The magnetic field of active region 11158 during the 2011 February 12-17 flares: Differences between photospheric extrapolation and coronal forward-fitting methods*, ApJ 785, 34.
- Aschwanden, M.J., Xu, Y., Jing, J. 2014b, ApJ 797, 50. *Global energetics of solar flares. I. Magnetic energies*

- Aschwanden, M.J. 2015, *Magnetic energy dissipation during the 2014 March 29 solar flare*, ApJ 804, L20.
- Aschwanden, M.J., Schrijver, C.J., and Malanushenko, A. 2015, *Blind stereoscopy of the coronal magnetic field*, SoPh 290, 2765.
- Aschwanden, M.J. 2016, ApJSS 224, 25. *The vertical current approximation nonlinear force-free field code - Description, performance tests, and measurements of magnetic energies dissipated in solar flares*
- Aschwanden, M.J., Reardon, K., and Jess, D.B. 2016, *Tracing the chromospheric and coronal magnetic field with AIA, IRIS, IBIS, and ROSA data*, ApJ 826, 61.
- Aschwanden, M.J. and Peter, H. 2017, ApJ 840, 4. *The width distribution of loops and strands in the solar corona - Are we hitting rock bottom*
- Aschwanden, M.J. 2019, *New Millennium Solar Physics*, Section 11.8, New York: Springer, (in press), http://www.lmsal.com/~aschwand/bookmarks_books2.html.
- Berger, M.A. and Asgari-Targhi, M. 2009, ApJ 705, 347. *Self-organized braiding and the structure of coronal loops*
- Berger, M.A., Asgari-Targhi, M., and DeLuca, E.E. 2015, J. Plasma Phys. 81/4, 395810404. *Self-organized braiding in solar coronal loops*
- Bourdin, P.A., Bingert, S., and Peter, H. 2013, A&A 555, A123. *Observationally driven 3D MHD model of the solar corona above an active region*
- Bourdin, P.A., Bingert, S., and Peter, H. 2015, A&A 580, A72. *Coronal energy input and dissipation in a solar active region 3D MHD model*
- Boyd, T.J.M., Sanderson, J.J.: 2003, *The Physics of Plasmas*, Cambridge University Press, Cambridge, p.102.
- Brooks, D.H., Warren, H.P., Ugarte-Urra, I., and Winebarger, A.R. 2013, ApJ 772, L19. *High Spatial Resolution Observations of Loops in the Solar Corona*
- Brooks, D.H., Reep, J. W., and Warren, H.P. 2016, ApJ 826, L18. *Properties and Modeling of Unresolved Fine Structure Loops Observed in the Solar Transition Region by IRIS*
- Candelaresi, S., Pontin, D.I., Yeates, A.R., et al. 2018, ApJ 864, 157. *Estimating the rate of field line braiding in the solar corona by photospheric flows*
- Cirtain, J.W., Golub, L., Winebarger, A.R. 2013, *Energy release in the solar corona from spatially resolved magnetic braids*.
- Dahlburg, R.B., Einaudi, G., Taylor, B.D., et al. 2016, ApJ 817, 47. *Observational signatures of coronal loop heating and cooling driven by footpoint shuffling*
- Démoulin, P., Pariat, E., and Berger, M.A. 2006, *Basic properties of mutual magnetic helicity*, SoPh 233, 3.
- DeRosa, M.L., Schrijver, C.J., Barnes, G., et al. 2009, ApJ 696, 1780. *A critical assessment of nonlinear force-free field modeling of the solar corona for active region 10953*.
- Gary, G.A. and Moore, R.L. 2004, ApJ 611, 545. *Eruption of a Multiple-Turn Helical Magnetic Flux Tube in a Large Flare: Evidence for External and Internal Reconnection That Fits the Breakout Model of Solar Magnetic Eruptions*

- Gold, T. and Hoyle, R. 1960, MNRAS 120, 89. *On the origin of solar flares*
- Hansteen, V., Guerreiro, N., de Pontieu, B., et al. 2015, ApJ 811, 106. *Numerical simulations of coronal heating through footpoint braiding*
- Hassanin, A. and Kliem, B. 2016, ApJ 832, 106. *Helical kink instability in a confined solar eruption*
- Hood, A.W. and Priest, E.R. 1979, *Kink instability of solar coronal loops as the cause of solar flares*, SoPh 64, 303.
- Hood, A.W. and Priest, E.R. 1981, *Critical conditions for magnetic instabilities in force-free coronal loops*, Geophys. and Astrophysical Fluid Dynamics 17(3-4), 297.
- Huang, Z., Xia, L., Nelson, C.J., et al. 2018, ApJ 854, 80. *Magnetic braids in eruptions of a spiral structure in the solar atmosphere*
- Isenberg, P.A. and Forbes, T.G. 2007, *A 3-D line-tied magnetic field model for solar eruption*, ApJ 670, 1453.
- Kliem, B. and Török, T. 2006, *Torus instability*, Phys.Rev.Lett. 96, 255002.
- Kliem, B. et al. 2010, *Reconnection of a kinking flux rope triggering the ejection of a microwave and hard X-ray source. II. Numerical modeling*, SoPh 266, 91.
- Kniznik, K.J., Antiochos, S.K., and DeVore, C.R. 2017, ApJ 835, 85. *The role of magnetic helicity in structuring the solar corona*
- Koleva, K., Madjarska, M.S., Duchlev, P., et al. 2012, A&A 540, A127. *Kinematics and helicity evolution of a loop-like eruptive prominence*
- Kumar, P., Srivastava, A.K., Filippov, B., and Uddin, W. 2010, SoPh 266, 39. *Multiwavelength study of the M8.9/3B solar flare from AR NOAA 10960*
- Kumar, P., Cho, K.S., Bong, S.C., et al. 2012, *Initiation of coronal mass ejection and associated flare caused by helical kink instability observed by SDO/AIA*
- Liu, Y. and Schuck, P.W. 2012, ApJ 761, 105. *Magnetic energy and helicity in two emerging active regions in the Sun*
- Longcope, D.W., Ravindra, B., and Barnes, G. 2007. ApJ 668, 571. *Determining the source of coronal helicity through measurements of braiding and spin helicity fluxes in active regions*
- Malanushenko, A., Yusuf, M.H., and Longcope, D.W. 2011, ApJ 736, 97. *Direct measurements of magnetic twist in the solar corona*
- Malanushenko, A., Schrijver, C.J., DeRosa, M.L., Wheatland, M.S., and Gilchrist, S.A. 2012, ApJ 756, 153. *Guiding nonlinear force-free modeling using coronal observations: First results using a quasi-grad-Rubin scheme*
- Morton, R.J., and McLaughlin, J.A. 2013. A&A 553, L10. *Hi-C and AIA observations of transverse magnetohydrodynamic waves in active regions*
- Pant, V., Datta, A., and Banerjee, D. 2015, ApJ 801, L2. *Flows and waves in braided solar coronal magnetic structures*

- Parker, E.N. 1988, ApJ 330, 474, *Nanoflares and the solar X-ray corona*
- Peter, H. 2015, Phil.Trans.Royal Soc. A 373/2042, 20150055. *What can large-scale MHD numerical experiments tell us about coronal heating?*
- Peter, H., Bingert, S., Klimchuk, J.A., de Forest, C., Cirtain, J.W., Golub, L., Winebarger, A. R., Kobayashi, K., and Korreck, K.E. 2013, A&A 556, 104. *Structure of solar coronal loops: from miniature to large-scale*
- Pontin, D.I., Wilmot-Smith, A.L., Hornig, G., et al. 2011, A&A 525, A57. *Dynamics of braided coronal loops. II. Cascade to multiple small-scale reconnection events*
- Pontin, D.I. and Hornig, G. 2015, ApJ 805, 47. *The structure of current layers and degree of field-line braiding in coronal loops*
- Pontin, D.I., Janvier, M., Tiwari, S.K., Galsgaard, K., et al. 2017, *Observational signatures of energy release in braided coronal loops*
- Portier-Fozzani, F., Aschwanden, M., Démoulin, P. et al. 2001, *Measurement of coronal magnetic twist during loop emergence of NOAA 8069*
- Priest, E.R.: 1982, *Solar Magnetohydrodynamics*, Geophysics and Astrophysics Monographs Volume 21, D. Reidel Publishing Company, Dordrecht, p.125.
- Priest, E. 2014, *Magnetohydrodynamics of the Sun*, Cambridge, UK: Cambridge University Press, p.111.
- Prior, C. and Berger, M.A. 2012, SoPh 278, 323. *On the shape of force-free field lines in the solar corona*
- Prior, C. and Yeates, A.R. 2016a, A&A 587, A125. *Twisted versus braided magnetic flux ropes in coronal geometry. I. Construction and relaxation*
- Prior, C. and Yeates, A.R. 2016b, A&A 591, A16. *Twisted versus braided magnetic flux ropes in coronal geometry. II. Comparative behaviour*
- Raouafi, N.E. 2009, ApJ 691, L128. *Observational evidence for coronal twisted flux rope*
- Reale, F., Orlando, S., Guarrasi, M., et al. 2016, ApJ 830, 21. *3-D MHD modeling of twisted coronal loops*
- Ritchie, M.L., Wilmot-Smith, A.L., and Hornig, 2016, *The dependence of coronal loop heating on the characteristics of slow photospheric motions*
- Rust, D.M. and Kumar, A. 1996, ApJ 464, L199. *Evidence for helically kinked magnetic flux ropes in solar eruptions*
- Sandman, A.W., Aschwanden, M.J., DeRosa, M.L., et al. 2009, *Comparison of STEREO/EUVI loops with potential magnetic field models*, SoPh 259, 1.
- Sandman, A.W. and Aschwanden, M.J. 2011, *A new method for modeling the coronal magnetic field with STEREO and submerged dipoles*, SoPh 270, 503.
- Sturrock, P.A.: 1994, *Plasma Physics. – An Introduction to the Theory of Astrophysical, Geophysical and Laboratory Plasmas*, Cambridge University Press, Cambridge, p.216.
- Thalmann, J.K., Tiwari, S.K., and Wiegmann, T. 2014, ApJ 780, 102, *Force-free field modeling of twist and braiding-induced magnetic energy in an active region corona*

- Tiwari, S.K., Alexander, C.E., Winebarger, A.R., et al. 2014, *Trigger mechanism of solar subflares in a braided coronal magnetic structure*
- Tiwari, S.K., Moore, R.L., Winebarger, A.R., and Alpert, S.E. 2016, ApJ 816, 92. *Transition-region/Coronal Signatures and Magnetic Setting of Sunspot Penumbra Jets: Hinode (SOT/FG), Hi-C, and SDO/AIA Observations*
- Török, T. and Kliem, B. 2003, *The evolution of twisting coronal magnetic flux tubes*, A&A 406, 1043.
- Török, T., Berger, M.A., and Kliem, B. 2010, A&A 516, A49. *The writhe of helical structures in the solar corona*
- Tritschler, A., Rimmele, T.T., Berukoff, S., et al. 2016, Astron.Nachrichten 337/10, 1064. *Daniel K. Inouye Solar Telescope: High-resolution of the dynamic Sun*
- van Ballegooijen, A.A., Asgari-Targhi, M., and Berger, M.A. 2014, *On the relationship between photospheric footpoint motions and coronal heating in solar active regions*
- van Ballegooijen, A.A., Asgari-Targhi, M., and Voss, A. 2017, ApJ 849, 46. *The heating of solar coronal loops by Alfvén wave turbulence*
- Warren, H.P., Winebarger, A.R., and Brooks, D.H. 2012, *A systematic survey of high-temperature emission in solar active regions*, ApJ 759, 141.
- Warren, H.P., Crump, N.A., Ugarte-Urra, I., Sun, X., Aschwanden, M.J., and Wiegmann, T. 2018, ApJ 860, 46. *Toward a quantitative comparison of magnetic field extrapolations and observed coronal loops*
- Wedemeyer-Böhm, S., Scullion, E., Steiner, O., et al. 2012, Nature 486, Issue 7404, 505. *Magnetic tornadoes as energy channels into the solar corona*
- Wiegmann T., Inhester, B., and Sakurai, T. 2006, SoPh 233, 315. *Preprocessing of Vector Magnetograph Data for a Nonlinear Force-Free Magnetic Field Reconstruction*
- Wiegmann, T., Neukirch, T., Nickeler, D.H., Solanki, S.K., Barthol, et al. 2017, ApJSS 229, 18. *Magneto-static Modeling from Sunrise/IMaX: Application to an Active Region Observed with Sunrise II*
- Wilmot-Smith, A.L., Hornig, G., and Pontin, D.I. 2009, ApJ 704, 1288. *Magnetic braiding and quasi-separatrix layers*
- Wilmot-Smith, A.L., Pontin, D.I., and Hornig, G. 2010, A&A 516, A5. *Dynamics of braided coronal loops*
- Wilmot-Smith, A.L., Pontin, D.I., Yeates, A.R., et al. 2011, A&A 536, A67. *Heating of braided coronal loops*
- Winebarger, A.R., Walsh, R.W., Moore, R., et al. 2013, ApJ 771, 21. *Detecting nanoflare heating events in subarcsecond inter-moss loops using Hi-C*
- Winebarger, A.R., Cirtain, J., Golub, L., and DeLuca, E. 2014, ApJ 787, L10. *Discovery of finely structured dynamic solar corona observed in the Hi-C telescope*
- Yeates, A.R., Hornig, G., and Wilmot-Smith, A.L. 2010, Phys.Rev.Lett. 105/8, 085002. *Topological constraints on magnetic relaxation*
- Yeates, A.R., Bianchi, F., Welsch, B.T., et al. 2014, A&A 564, A131. *The coronal energy input from magnetic*

braiding

Table 1: Data selection parameters (observation date and time, heliographic position of center of image, field-of-view of image in units of solar radii), and data analysis results from AIA/SDO and HMI/SDO data: ratio of nonpotential to potential energy (E_{NP}/E_P), nonpotentiality angle between nonpotential and potential field μ , number of helical twist turns (N_{twist}), helical twist rotation angle φ , based on the VCA-NLFFF forward-fitting code.

#	Observation date and time (UT)	Heliographic position	Field of view FOV (R_\odot)	Energy ratio E_{NP}/E_P	Nonpot. angle μ_{NP} (deg)	Number of twist N_{twist}	Rotation angle φ (deg)
1	20100619 012742	N29E19	0.335	1.044	11.9°	0.10± 0.06	34° ± 19°
2	20100621 011627	N26W07	0.408	1.039	11.2°	0.11± 0.09	40° ± 33°
3	20100723 143256	S27E23	0.419	1.058	13.6°	0.14± 0.09	49° ± 33°
4	20100929 232134	N21W21	0.481	1.064	14.2°	0.18± 0.12	63° ± 42°
5	20110121 134056	N21E04	0.523	1.085	16.3°	0.12± 0.12	42° ± 43°
6	20110131 105511	S24E35	0.408	1.061	13.8°	0.14± 0.10	51° ± 37°
7	20110212 150157	S21E19	0.367	1.034	10.4°	0.08± 0.07	29° ± 24°
8	20110411 113035	N17E34	0.533	1.087	16.4°	0.17± 0.11	61° ± 41°
9	20110415 004705	N19W11	0.512	1.091	16.8°	0.17± 0.13	61° ± 47°
10	20110419 130206	N15W05	0.512	1.078	15.6°	0.13± 0.09	45° ± 32°
11	20110702 030812	N15E22	0.388	1.087	16.5°	0.16± 0.10	57° ± 34°
12	20110725 090557	N25W15	0.575	1.047	12.2°	0.14± 0.12	48° ± 41°
13	20110821 115609	N15E05	0.575	1.055	13.2°	0.12± 0.10	42° ± 34°
14	20111108 184444	N20W03	0.575	1.145	20.8°	0.19± 0.13	69° ± 47°
15	20111110 110329	N21W26	0.502	1.096	17.2°	0.13± 0.11	48° ± 38°
mean			0.47±0.08	1.07± 0.03	14.7° ± 2.8°	0.14±0.03	49° ± 11°

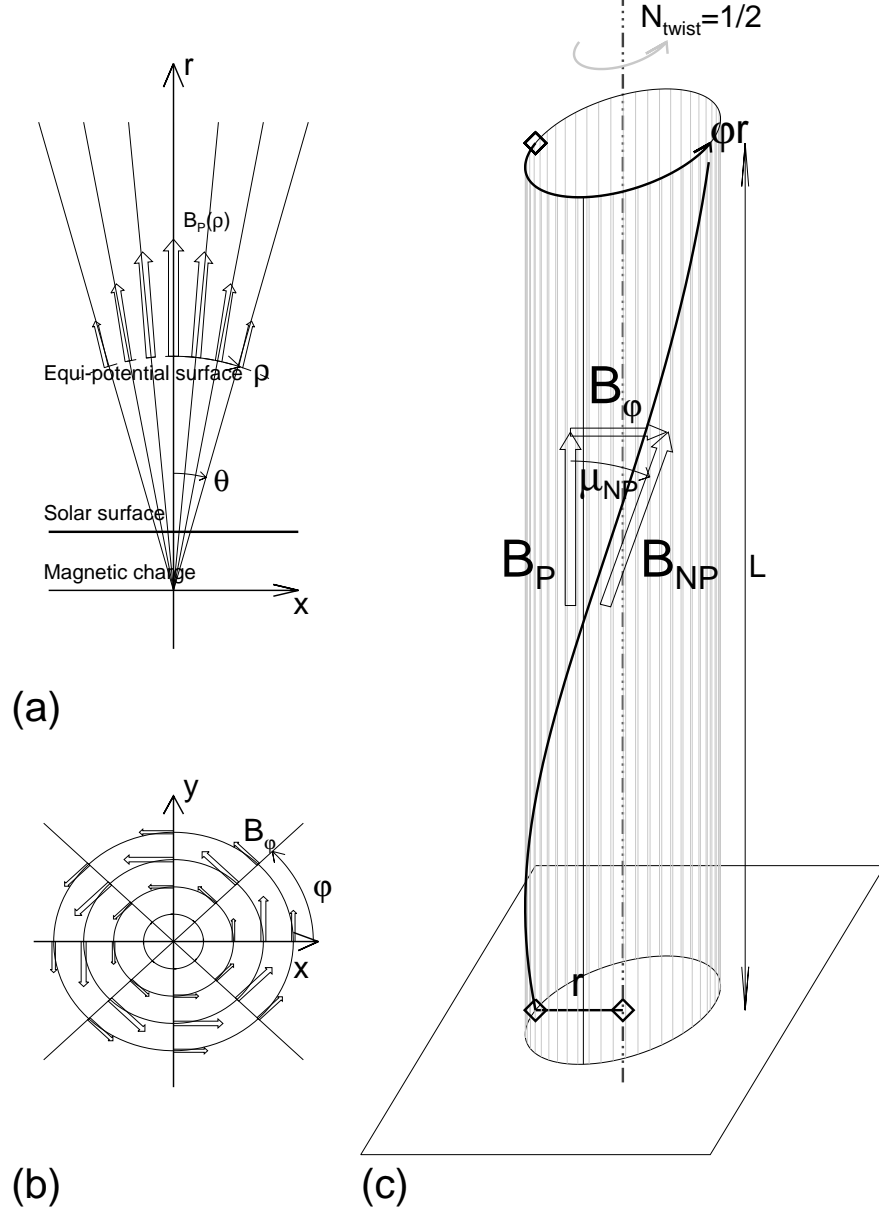


Fig. 1.— Geometric concept of vertical current approximation model: (a) A magnetic charge is buried below the solar surface, with radial field lines B_r pointing away with inclination angles θ ; (b) Top view onto x-y plane with azimuthal field component B_ϕ indicated; (c) The relationship of the radial potential field $B_r = B_P$, the nonpotential field B_{NP} , and the azimuthal field component B_ϕ , which are distorted by a nonpotentiality angle μ_{NP} in a helically twisted flux tube. The twist corresponds to a half turn ($N_{twist} = 0.5$) over a length L .

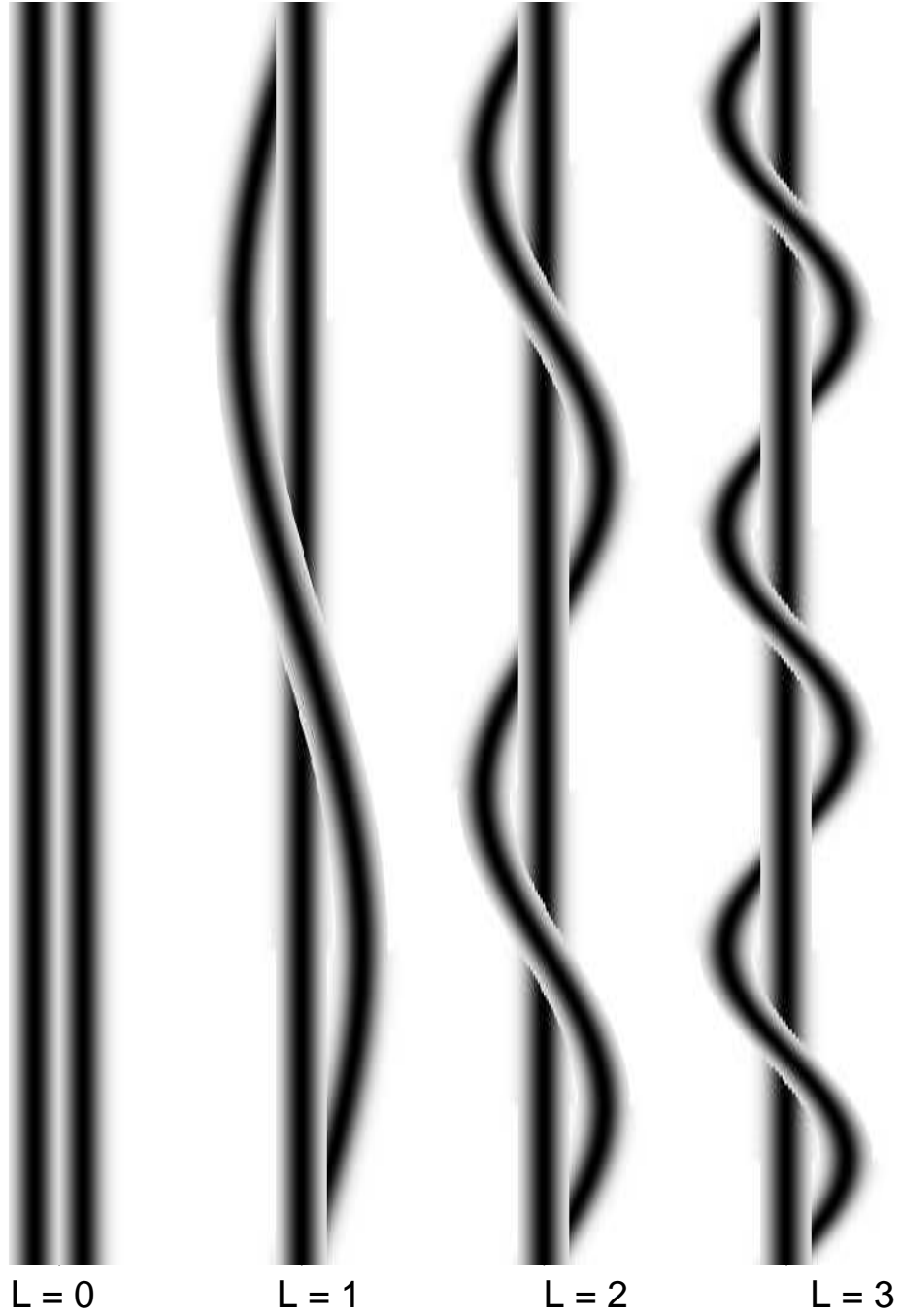


Fig. 2.— Four pairs of loops with different Linkage numbers ($L=0, 1, 2, 3$). The untwisted case $L = 0$ corresponds to a potential field model, $L = 1$ to a twisted loop near the torus instability, and two cases of braided loops ($L = 2, 3$) that are unstable.

20111108_184444, time step=1, Catalog=event_runA.txt

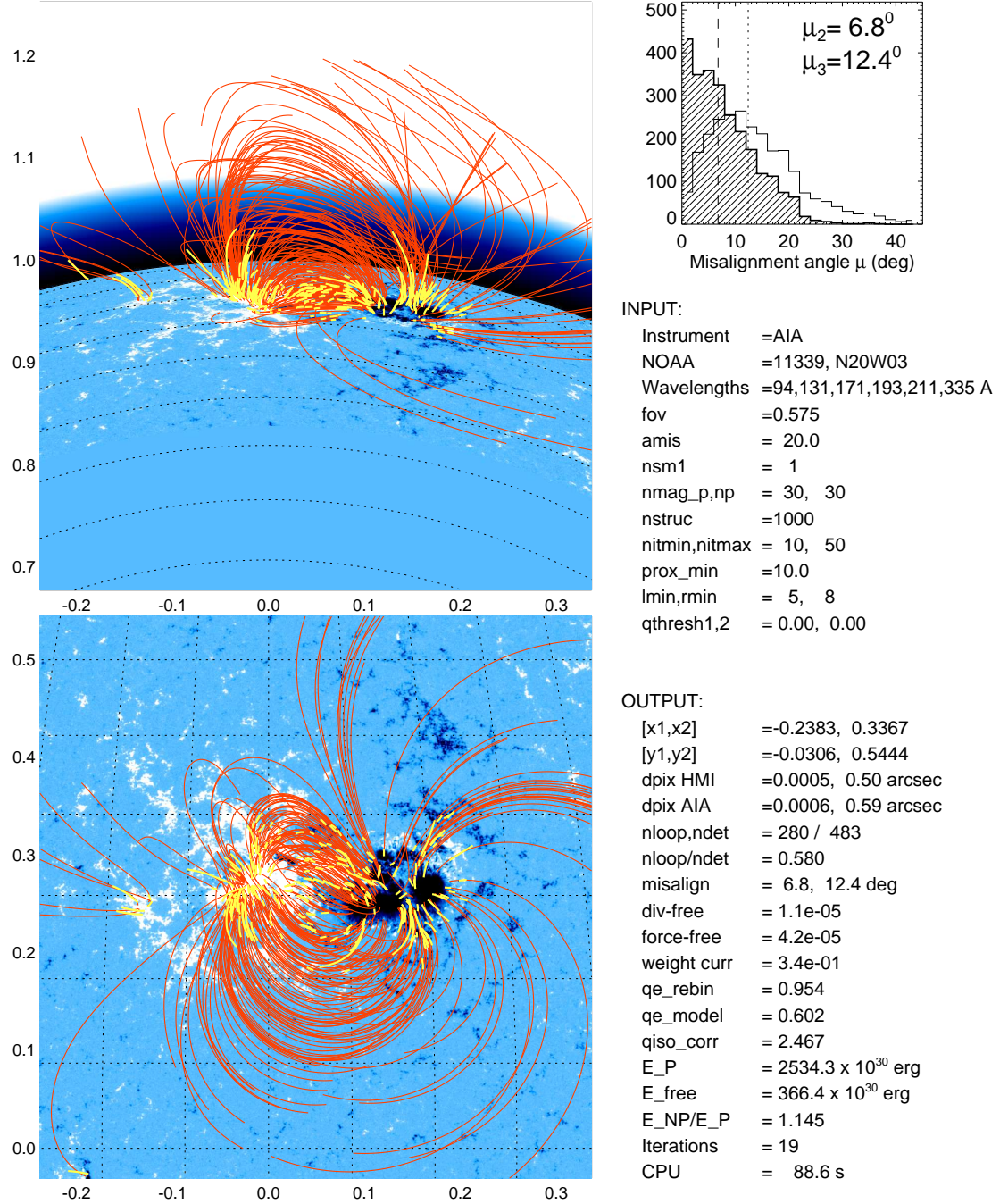


Fig. 3.— Magnetic field model obtained from forward-fitting of the VCA-NLFFF code to AIA/SDO and HMI/SDO data of event #14, observed on 2011 November 08, 18:44:44 UT, with heliographic position N20W03 at the image center. *Bottom left*: Automatically traced loops in AIA/SDO in all coronal wavelength bands (yellow), with the best fitting magnetic field lines (red curves) overlaid on the HMI magnetogram (blue). *Top left*: 3-D magnetic field configuration rotated by 90° as it would be seen from a top view from far above the solar north pole. *Top right*: Histogram of 2-D (μ_2) and 3-D (μ_3) misalignment angles between the observed loop directions (yellow curves) and the theoretical magnetic field model (red curves), each measured in 7 segments of the 280 traced loops.

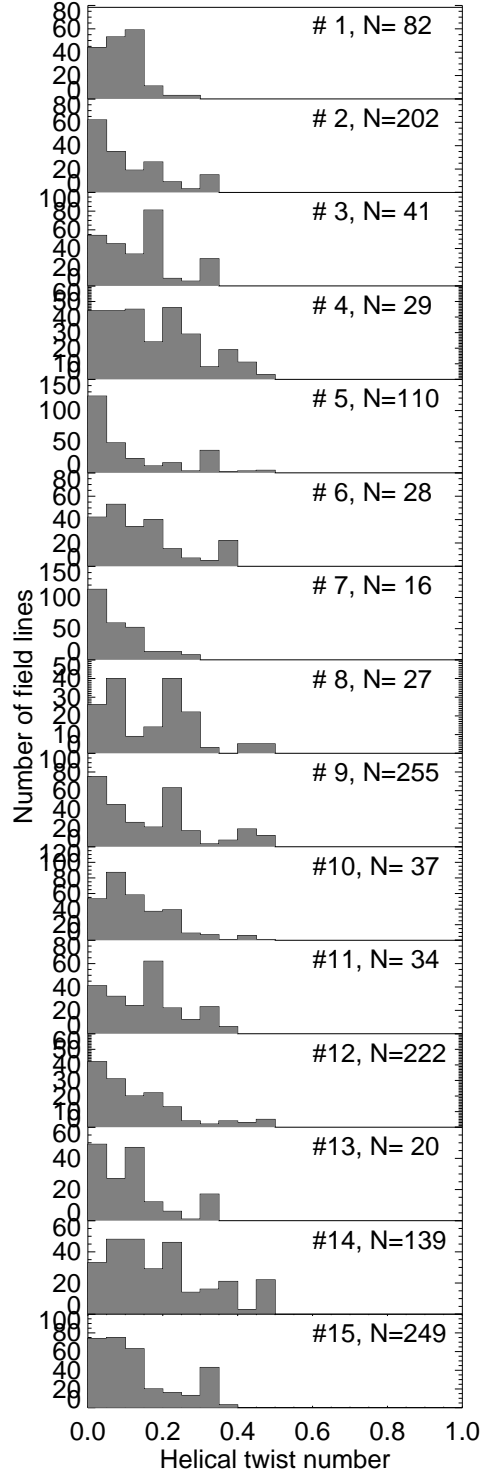


Fig. 4.— Statistical distributions of helical twist numbers N_{twist} shown separately for each of the 15 active regions listed in Table 1. The number of measured field lines is given in the top right corner. Note that the helical twist number never exceeds a value of a half turn (i.e., $N_{twist} \lesssim 0.5$).